

FoRA: Fisher-orthogonal Rank Adaptation for Parameter-Efficient Fine-Tuning

Juneyoung Park¹, Seongbae Lee¹, Han-Sang Lee², Kyuho Lee², Minjae Kim²,
Seunghyeon Hyeon^{2*}, KIDUK KWON^{2*}, Seongwan Kim^{1*}, Jaeho Lee^{1*}

¹OptAI Inc, ²LG Uplus

Abstract

Parameter-efficient fine-tuning (PEFT) has largely focused on LoRA and its accuracy-oriented variants, leaving the original goal of reducing trainable parameters has received comparatively little attention. We introduce FoRA, which revisits this goal by reducing the number of adapted layers rather than adapter rank. FoRA selects task-informative layers via a single-pass diagonal Fisher score (under 1% of training cost) and trains the LoRA down-projection at selected layers on the Stiefel manifold, preserving column orthonormality and effective rank. FoRA consistently outperforms LoRA and DoRA at half their parameter budget, and falls within 0.7–0.8 accuracy points of AdaLoRA at one-quarter its parameter count, across five LLaMA-family backbones. Cross-architecture experiments on twelve backbones from the LLaMA, Qwen3, and Gemma families confirm consistent gains from 270M to 32B parameters. The two components combine super-additively: Fisher selection alone matches rank reduction at the same budget, while the Stiefel constraint provides the decisive additional gain.

Code — <https://github.com/crinex/FoRA>

1 Introduction

LoRA (Hu et al., 2022) has become the de facto standard for parameter-efficient fine-tuning (PEFT) by freezing the pretrained weights and learning only a small low-rank update $\Delta W = BA$. Subsequent work, including DoRA (Liu et al., 2024a), rsLoRA (Kalajdzievski, 2023), and PiSSA (Meng et al., 2024), has focused on improving accuracy

or training dynamics under a fixed parameter budget. Recent studies report that the effective rank of trained LoRA adapters often falls well below the nominal rank (Biderman et al., 2024; Hayou et al., 2024), suggesting that gains along this accuracy-oriented axis are narrowing.

The original goal of LoRA, parameter efficiency itself, has received comparatively little attention. Reducing parameters in the LoRA family typically means lowering the rank r . This directly shrinks the subspace each adapter can represent, losing expressiveness at the very layers where adaptation is most needed. Layer-level methods such as LISA (Pan et al., 2024) and LoRA-drop (Zhou et al., 2024) attempt selective adaptation, but rely on stochastic layer sampling or post-hoc pruning, both of which add overhead or require a full training pass before selection is fixed. AdaLoRA (Zhang et al., 2023) redistributes per-layer rank dynamically but recomputes SVD-based importance at every step and introduces multiple schedule hyperparameters.

We take a different approach: rather than cutting the rank, we reduce the number of adapted layers while preserving per-adapter rank intact. Adapting only a small set of information-rich layers yields comparable or better performance at half the parameter count. We identify these layers using an empirical diagonal Fisher score computed in a single forward-backward pass before fine-tuning begins (below 1% of training cost) and hold the selection fixed throughout training.

Reducing the layer count also concentrates task pressure on the remaining adapters. To ensure each adapter fully uses its capacity, we constrain the LoRA down-projection B to the Stiefel manifold of column-orthonormal matrices via Cayley parametrization (Wen and Yin, 2013). This enforces that all r orthogonal directions of each adapter are utilized, preventing the spectral collapse reported for unconstrained LoRA (Biderman

*Corresponding authors: Seunghyeon Hyeon, KIDUK KWON, Seongwan Kim, Jaeho Lee.

¹OptAI Inc.: {jyoung.park, sbae.lee, swan.kim, jaeho.lee}@opt-ai.kr

²LG Uplus: {hansanglee, kyuholee, minjaekim, sheon, kwonkiduk}@lguplus.co.kr

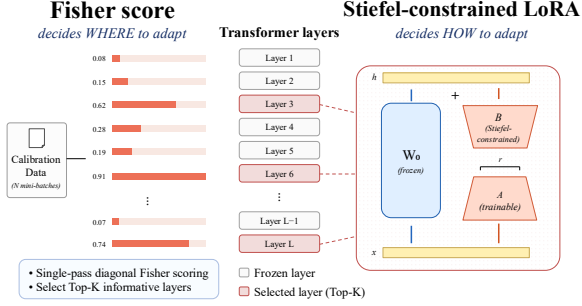


Figure 1: Overview of FoRA. FoRA uses calibration data to score Transformer layers with diagonal Fisher information, selects the Top-K informative layers for adaptation, and applies Stiefel-constrained LoRA only to those layers while keeping the rest frozen.

et al., 2024; Hayou et al., 2024).

We combine these two ideas into **FoRA** (Fisher-orthogonal Rank Adaptation): Fisher decides *where* to adapt, and the Stiefel constraint shapes *how* that capacity is used. The two components are orthogonal in design and combine super-additively, as our ablation confirms.

Our contributions are: (i) a static Fisher-based layer selection criterion that halves the adapter layer count at below 1% calibration cost, enabling FoRA to outperform LoRA and DoRA at half their parameter budget and match AdaLoRA within 0.7–0.8 accuracy points at one-quarter its budget; (ii) a Stiefel-constrained adapter that restores effective rank from 0.71 to 0.88 of the nominal rank and combines super-additively with layer selection; and (iii) consistent validation across twelve backbones from the LLaMA, Qwen3, and Gemma families at scales from 270M to 32B parameters.

2 Related Work

LoRA and its variants. LoRA (Hu et al., 2022) freezes the pretrained weight W_0 and learns a low-rank update $\Delta W = BA$. Follow-up methods improve accuracy or training stability at a fixed parameter budget: DoRA (Liu et al., 2024a) decomposes updates into magnitude and direction; rsLoRA (Kalajdzievski, 2023) corrects rank scaling; PiSSA (Meng et al., 2024) initializes from the dominant singular vectors; LoRA+ (Hayou et al., 2024) uses asymmetric learning rates for A and B . These methods can be combined with base-model quantization, as in QLoRA (Dettmers et al., 2023). Despite these improvements, the effective rank of trained adapters is often substantially below the nominal rank r (Biderman et al., 2024; Hayou

et al., 2024), limiting further gains along this axis.

Selective layer-level fine-tuning. AdaLoRA (Zhang et al., 2023) dynamically redistributes per-layer rank using SVD-based importance scores recomputed at every step. LISA (Pan et al., 2024) samples a random layer subset at each iteration, and LoRA-drop (Zhou et al., 2024) prunes adapters post-hoc by output magnitude. All three determine the layer set during or after training, incurring calibration overhead or requiring a full pass before selection is fixed. FoRA instead computes a Fisher score in a single forward-backward pass before fine-tuning begins and holds the selection static throughout training.

Orthogonal and manifold constraints. OFT (Qiu et al., 2023) and BOFT (Liu et al., 2024b) constrain weight updates to orthogonal transformations that preserve hyperspherical energy between neuron activations. VeRA (Kopiczko et al., 2024) takes an extreme compression approach by sharing a single pair of fixed random matrices across all layers and learning only per-layer scaling vectors, locking each adapter to a fixed random subspace while minimizing trainable parameters. In the LoRA family specifically, Park et al. (2025) optimize the down-projection B on the Stiefel manifold of column-orthonormal matrices via Cayley parametrization (Wen and Yin, 2013), showing that this constraint prevents spectral collapse and restores the effective rank of the adapter output.

Consequently, FoRA integrates static Fisher-based layer selection with Stiefel-constrained down-projections, efficiently optimizing both adapter placement and rank utilization simultaneously.

3 Method

Preliminaries. We use the standard LoRA (Hu et al., 2022) parametrization. For a pretrained linear weight $W_0 \in \mathbb{R}^{d_{\text{out}} \times d_{\text{in}}}$ in a transformer layer, LoRA freezes W_0 and adds a low-rank update

$$W = W_0 + \Delta W, \quad \Delta W = BA, \quad (1)$$

where $A \in \mathbb{R}^{r \times d_{\text{in}}}$, $B \in \mathbb{R}^{d_{\text{out}} \times r}$, and $r \ll \min(d_{\text{out}}, d_{\text{in}})$. We denote the set of L transformer layers by $\{\ell_1, \dots, \ell_L\}$ and the union of trainable adapter parameters at layer ℓ by $\theta_\ell = \{A_\ell, B_\ell\}$ across all target modules. Following Hu et al. (2023), the target modules at each adapted layer are the three self-attention projections $\{q, k, v\}$ and

the two MLP projections {up, down}, for a total of five projections per layer. Standard LoRA applies adapters to every layer, giving a trainable parameter count of $L \cdot M \cdot r(d_{\text{in}} + d_{\text{out}})$ with M target modules per layer. Our goal is to reduce the number of layers that carry adapters while preserving the per-adapter capacity.

Fisher-based layer selection. We measure the importance of layer ℓ to the task using a block-diagonal empirical Fisher score restricted to the parameters of that layer,

$$F_\ell = \frac{1}{N} \sum_{n=1}^N \sum_{\theta \in \theta_\ell^{\text{base}}} \|\nabla_{\theta} \mathcal{L}(x_n, y_n)\|^2, \quad (2)$$

where $\theta_\ell^{\text{base}}$ are the base-model parameters of layer ℓ (not the adapter), \mathcal{L} is the task loss, and N is the number of mini-batches used for estimation. Equation (2) corresponds to the empirical Fisher diagonal trace per layer, which serves as a positive semi-definite curvature proxy that is invariant to per-layer reparametrization (Amari, 1998). We compute F_ℓ once before training, using a single forward-backward pass over N mini-batches with the base model, and select

$$\mathcal{S} = \text{TopK}(\{F_\ell\}_{\ell=1}^L, K), \quad (3)$$

the index set of the K layers with the highest scores. Adapters are inserted only at layers in \mathcal{S} , and \mathcal{S} is held fixed for the entire training run. The cost is dominated by N forward-backward passes over the base model, below one percent of the full training budget. We use the empirical Fisher (gradients on observed labels) rather than the true Fisher; this bias affects all layers comparably and does not change the relative ranking used for selection (Kunstner et al., 2019).

Stiefel-constrained adapter training. For each selected layer $\ell \in \mathcal{S}$, we constrain the down-projection B_ℓ to lie on the Stiefel manifold of column-orthonormal matrices, building on prior work that introduced this constraint for LoRA (Park et al., 2025).

$$\text{St}(d_{\text{out}}, r) = \{ B \in \mathbb{R}^{d_{\text{out}} \times r} : B^\top B = I_r \}. \quad (4)$$

This drives every rank- r adapter to span r orthogonal directions in the output space. The structural consequence is stronger than rank preservation alone, as the following lemma makes precise.

Lemma 1 *If $B \in \text{St}(d_{\text{out}}, r)$, then for every $A \in \mathbb{R}^{r \times d_{\text{in}}}$ the singular values of BA coincide with those of A :*

$$\sigma_i(BA) = \sigma_i(A) \quad \text{for all } i = 1, \dots, r.$$

A short proof is given in Appendix C. The lemma implies $\text{rank}(\Delta W) = \text{rank}(A)$, and more importantly, the entropy-based effective rank $\text{erank}(BA) = \text{erank}(A)$. The Stiefel constraint eliminates structural collapse on the down-projection side, reducing ΔW effective-rank preservation to the optimization of A alone. Crucially, maintaining strict column-orthonormality ($B^\top B = I_r$) acts as an implicit regularizer; the resulting geometric shielding prevents magnitude distortion or directional bias in gradients backpropagated to A . This stabilizes A 's Euclidean optimization and prevents rapid singular value decay, effectively mitigating the spectral collapse widely reported in unconstrained LoRA (Biderman et al. (2024); Hayou et al. (2024)), as validated in Section 5.3. This mechanism is empirically validated through our spectral analysis in Section 5.3. We maintain the constraint throughout training using the Cayley parametrization (Wen and Yin, 2013). Let $G_\ell = \partial \mathcal{L} / \partial B_\ell$ be the Euclidean gradient. We construct the skew-symmetric direction

$$\begin{aligned} W &= \widehat{W} - \widehat{W}^\top, \\ \widehat{W} &= G_\ell B_\ell^\top - \frac{1}{2} B_\ell B_\ell^\top G_\ell B_\ell^\top, \end{aligned} \quad (5)$$

which is the Riemannian gradient of \mathcal{L} on $\text{St}(d_{\text{out}}, r)$ at B_ℓ (Wen and Yin, 2013). Given W and a step size α , the Cayley update is

$$\begin{aligned} Q &= \left(I - \frac{\alpha}{2} W \right)^{-1} \left(I + \frac{\alpha}{2} W \right), \\ B^{(t+1)} &= Q B^{(t)}, \end{aligned} \quad (6)$$

which preserves $B^\top B = I_r$ exactly when computed in real arithmetic. We solve Eq. (6) with a fixed-point iteration in (d_{out}, r) space and periodically re-project B via QR to control numerical drift. Moment statistics follow Adam, giving Cayley-Adam for B_ℓ ; A_ℓ uses standard AdamW. Full pseudocode is in Appendix A. When implementing FoRA in a standard deployment scenario where adapter weights are fully merged into the base parameters prior to serving, the update simplifies directly to $W_l = W_{0,l} + B_l A_l$ for $l \in \mathcal{S}$. Because the non-selected layers ($l \notin \mathcal{S}$) remain

Model	Method	Params (M)	BoolQ	PIQA	HellaSwag	WinoGrande	ARC-e	ARC-c	OBQA	Avg.
LLaMA-3.2-1B	LoRA	15.2	62.8	74.5	61.8	61.2	61.1	35.0	39.0	56.5
	DoRA	15.4	63.0	74.6	61.6	60.8	61.9	35.6	37.4	56.4
	AdaLoRA	30.4	65.2	74.3	63.9	63.0	62.1	36.8	41.2	58.1
	FoRA (Ours)	7.6	63.9	73.5	62.0	62.8	64.0	36.7	39.2	57.4
LLaMA-3.2-3B	LoRA	33.0	78.1	76.8	71.0	65.7	66.2	41.0	42.2	63.0
	DoRA	33.5	77.8	76.4	71.8	64.6	61.2	37.8	41.0	61.5
	AdaLoRA	66.1	78.2	77.9	74.8	71.6	74.2	45.7	43.0	66.5
	FoRA (Ours)	16.5	71.8	77.5	72.8	71.8	69.7	42.3	41.6	64.0
LLaMA-2-7B	LoRA	56.1	81.3	77.2	71.2	66.5	62.8	37.0	45.0	63.1
	DoRA	57.0	81.6	77.5	71.6	66.9	63.1	37.3	45.4	63.3
	AdaLoRA	112.2	81.7	80.2	76.2	71.8	76.0	46.8	45.8	68.4
	FoRA (Ours)	28.0	79.7	78.9	74.0	71.3	75.4	46.5	44.8	67.2
LLaMA-3.1-8B	LoRA	56.6	81.2	79.3	74.0	69.9	59.1	40.1	44.6	64.0
	DoRA	57.4	80.2	78.7	73.9	67.5	63.3	40.4	44.8	64.1
	AdaLoRA	113.3	83.2	81.6	79.6	76.0	75.4	50.0	46.0	70.3
	FoRA (Ours)	28.3	84.2	82.1	80.3	77.2	76.5	50.2	45.1	70.8
LLaMA-2-13B	LoRA	87.8	79.3	78.9	75.8	69.3	59.5	39.0	46.6	64.0
	DoRA	89.2	80.9	78.7	75.9	69.0	57.9	38.8	47.6	64.1
	AdaLoRA	174.4	83.5	82.0	80.1	75.5	75.8	49.5	44.8	70.2
	FoRA (Ours)	43.9	84.1	82.2	81.4	76.8	75.4	51.0	46.8	71.1

Table 1: Accuracy on the seven-task commonsense reasoning benchmark for five LLaMA-family backbones across two model generations. Params (M) is the number of trainable parameters in millions. FoRA uses approximately half of the trainable parameters of LoRA-family methods while matching or exceeding their accuracy.

completely untouched, this zero-cost merging guarantees that FoRA introduces absolutely no additional inference latency, runtime memory overhead, or control-flow routing delays during text generation.

FoRA in summary. FoRA combines the two components above. Selection (Eq. 3) decides *where* the adapter capacity is spent, and the Stiefel constraint (Eq. 4) decides *how* that capacity is shaped. The two are orthogonal in the design sense: the Fisher selection step does not depend on the optimizer choice, and the Stiefel constraint does not depend on which layers are selected. We show in Section 4 that they combine super-additively, with the joint method outperforming either component alone by a margin larger than the sum of their individual gains.

4 Experiments

We design our experiments to verify three claims about the FoRA algorithm. First, FoRA matches or exceeds accuracy-oriented LoRA variants on standard benchmarks while using fewer trainable parameters (Section 4.2). Second, the Fisher-selection and Stiefel-constraint components contribute independently and combine super-additively, as a 2×2 ablation across twelve backbones makes apparent (Section 4.3). Third, the algorithm transfers across task domains and remains

effective when combined with weight quantization (Section 4.4, 4.5). Analyses of why the algorithm behaves this way are deferred to Section 5.

4.1 Experimental Setup

Models. We evaluate on twelve open-weight backbones spanning three families and base-model parameter counts from 270M to 32B: Gemma-3-270M, Gemma-3-1B, Gemma-2-9B, Gemma-2-27B; Qwen3-0.6B-Base, Qwen3-1.7B, Qwen3-4B, Qwen3-8B, Qwen3-32B; LLaMA-3.2-3B, LLaMA-3.1-8B, and LLaMA-2-13B. All models are loaded in bf16. **Training data and tasks.** Following Hu et al. (2023), we fine-tune on the Commonsense-170K instruction tuning corpus, an aggregation of training sets from seven commonsense reasoning benchmarks: BoolQ (Clark et al., 2019), PIQA (Bisk et al., 2020), HellaSwag (Zellers et al., 2019), WinoGrande (Sakaguchi et al., 2020), ARC-easy and ARC-challenge (Clark et al., 2018), and OpenBookQA (Mihaylov et al., 2018). We report per-task accuracy and the mean. We additionally report WikiText-2 perplexity (Merity et al., 2017) as a measure of language-modeling preservation after task adaptation. For Section 4.4, we use the Alpaca instruction-tuning dataset (Taori et al., 2023).

Baselines. We compare against vanilla LoRA (Hu et al., 2022), DoRA (Liu et al., 2024a), rsLoRA

Model	Method	Fisher	Stiefel	Params (M)	BoolQ	PIQA	HellaSwag	WinoGrande	ARC-e	ARC-c	OBQA	Avg.
LLaMA-3.1-8B	LoRA-all	✗	✗	56.6	81.16	79.27	73.96	69.85	59.09	40.10	44.60	64.00
	FG-LoRA	✓	✗	28.3	81.53	80.30	77.45	71.74	67.34	44.03	45.00	66.77
	Stiefel-LoRA	✗	✓	56.6	82.97	81.18	77.47	75.06	68.98	44.20	45.60	67.92
	FoRA (Ours)	✓	✓	28.3	82.72	81.61	78.55	76.56	76.14	47.70	45.40	69.81
Qwen3-8B	LoRA-all	✗	✗	59.0	83.58	77.97	74.42	67.25	57.62	39.51	41.20	63.08
	FG-LoRA	✓	✗	29.5	83.85	78.18	75.87	67.80	60.44	40.10	44.40	64.38
	Stiefel-LoRA	✗	✓	59.0	82.48	78.84	76.47	69.93	66.92	45.56	40.80	65.86
	FoRA (Ours)	✓	✓	29.5	85.57	78.78	76.74	70.17	74.24	48.29	42.00	67.97
Gemma-2-27B	LoRA-all	✗	✗	154.5	83.33	79.92	78.33	72.77	58.08	37.80	47.00	65.32
	FG-LoRA	✓	✗	77.3	83.55	82.26	79.46	73.24	65.74	43.86	49.60	68.24
	Stiefel-LoRA	✗	✓	154.5	82.50	83.15	81.20	76.45	78.90	51.24	47.41	71.55
	FoRA (Ours)	✓	✓	77.3	81.13	84.28	83.98	78.69	87.79	65.87	47.40	75.59

Table 2: Per-task accuracy on the seven commonsense benchmarks for one representative backbone from each of the three model families. Params (M) is the trainable adapter parameter count. The complete per-backbone breakdown is given in Appendix B.

(Kalajdziewski, 2023), and AdaLoRA (Zhang et al., 2023). We additionally include two internal ablations to isolate the contribution of each FoRA component: *FG-LoRA*. We include two internal ablations: *FG-LoRA* (Fisher-guided top-K layers without Stiefel constraints) and *Stiefel-LoRA* ((Park et al., 2025); Stiefel constraints at every layer without selection). The latter represents prior work that introduced Stiefel-manifold optimization for LoRA; FoRA differs by combining this constraint with Fisher-based selective application.

Hyperparameters. For all methods we use rank $r = 32$, $\alpha = 64$, and target modules $\{q, k, v, \text{up}, \text{down}\}$ following Hu et al. (2023). FoRA additionally uses layer budget $K = L/2$ and Fisher batches $N = 128$; remaining FoRA-specific hyperparameters are listed in the Appendix. We report mean and standard deviation over three seeds. Hardware is $8 \times$ NVIDIA H200.

4.2 Main Results: Commonsense Reasoning

Table 1 compares FoRA against the LoRA family on the commonsense reasoning suite for five LLaMA-family backbones across two generations. FoRA consistently outperforms LoRA and DoRA across all backbones at half their parameter budget. Crucially, the relative gain over vanilla LoRA scales with model size (from +0.9 on 1B to +5.6 on 8B), supporting the hypothesis that larger models contain more layers that selective adaptation can skip without loss. Against AdaLoRA, which uses twice the parameter budget of LoRA, FoRA falls within 0.7–0.8 accuracy points on four of five models (LLaMA-3.2-1B, LLaMA-2-7B, LLaMA-3.1-8B, LLaMA-2-13B) while requiring only one-quarter of AdaLoRA’s trainable parameters (28.3M vs. 113.3M on LLaMA-3.1-8B). The independent

Method	Params (M)	MT-Bench
LoRA	159.9	5.70
DoRA	160.5	6.00
rsLoRA	159.9	5.82
FoRA (Ours)	80.0	6.15

Table 3: Instruction following on LLaMA-2-7B fine-tuned with Alpaca-52K (Taori et al., 2023), evaluated on MT-Bench (Zheng et al., 2023).

contributions of Fisher-based layer selection and the Stiefel constraint are analyzed in Section 4.3.

4.3 Ablation: Fisher Selection \times Stiefel Constraint

We isolate the two components of FoRA with a 2×2 ablation: Fisher selection (on or off) and Stiefel constraint (on or off). LoRA-all turns both off, FG-LoRA turns Fisher selection on, Stiefel-LoRA turns the Stiefel constraint on, and FoRA turns both on. Table 2 reports this ablation on one representative backbone from each family; full results across all twelve backbones are in Appendix B. FoRA achieves the best commonsense average on the majority of backbones, and is never worse than LoRA-all except on Gemma-3-270M, suggesting that the efficiency advantage scales with model size and is not specific to any architecture.

4.4 Instruction Following

To verify that FoRA generalizes beyond commonsense reasoning to a different task domain, we fine-tune LLaMA-2-7B on the 52K Alpaca instruction tuning corpus (Taori et al., 2023) and evaluate the resulting models on the MT-Bench protocol (Zheng et al., 2023) using GPT-4 as the judge. Table 3 reports the average MT-Bench score together with

Model	Method	Params (M)	MMLU
LLaMA-2-7B	QLoRA	56.1	41.0
	QDoRA	57.0	39.9
	QFoRA (Ours)	28.0	38.9
LLaMA-3.1-8B	QLoRA	56.6	38.7
	QDoRA	57.4	46.8
	QFoRA (Ours)	28.3	52.1

Table 4: MMLU accuracy when combining FoRA with 4-bit quantization (QFoRA) on LLaMA-2-7B and LLaMA-3.1-8B.

trainable parameter counts. LoRA, DoRA, and rsLoRA baselines are cited from Liu et al. (2024a).

The relative ordering observed in commonsense reasoning is preserved on instruction following. FoRA matches or exceeds the strongest baseline at a fraction of the trainable parameters, indicating that the gains from selective adaptation and rank-utilization preservation are not specific to multiple-choice classification tasks.

4.5 QFoRA: Combining FoRA with Quantization

Beyond reducing the number of trainable parameters, practitioners often need to reduce the memory footprint of the frozen base model itself. QLoRA (Dettmers et al., 2023) addresses this by quantizing the pretrained weights to 4-bit NF4 while keeping the LoRA adapter in higher precision. We verify that FoRA composes with this quantization scheme by replicating the QLoRA setup with the FoRA adapter, which we refer to as QFoRA, and compare against QLoRA and QDoRA (Liu et al., 2024a). Table 4 reports MMLU accuracy for LLaMA-2-7B and LLaMA-3.1-8B with the base model quantized to 4-bit.

While QFoRA underperforms QDoRA on the smaller LLaMA-2-7B backbone, which we attribute to the lower tolerance of highly constrained 7B architectures to the combined approximation noise of NF4 quantization and Cayley retractions, this limitation is rapidly overcome as model scale increases. On the more robust LLaMA-3.1-8B backbone, QFoRA achieves performance gains of +5.3 accuracy points over QDoRA and +17.4 accuracy points over QLoRA, despite using approximately half the trainable parameter budget. This reversal demonstrates that as base model capacity scales, FoRA’s joint mechanisms of Fisher-guided layer selection and Stiefel constraints become highly resilient to, and compatible with, low-

Config	Layers	Rank	Params (M)	PPL
LoRA (full)	28	32	33.0	7.469
LoRA, $r=16$	28	16	16.5	7.346
LoRA, $K=14$ random	14	32	16.5	7.279
FG-LoRA	14	32	16.5	7.381
FoRA (Ours)	14	32	16.5	7.035

Table 5: Parameter-matched comparison on LLaMA-3.2-3B (seed 42, $n_{\text{train}} = 4096$). All four budget- $P_0/2$ configurations have identical trainable parameter counts.

bit weight quantization, delivering Pareto-optimal memory and accuracy trade-offs.

5 Discussion

Section 4 showed that FoRA outperforms LoRA and DoRA at half their parameter budget, and falls within 0.7–0.8 accuracy points of AdaLoRA at one-quarter its budget. This section asks *why* the method works. We analyze it along five complementary axes: why layer reduction beats rank reduction at a matched parameter budget (Section 5.1), robustness to the layer budget K (Section 5.2), the Stiefel mechanism that preserves rank utilization and keeps output distributions close to base (Section 5.3), the empirical justification for the diagonal Fisher approximation (Section 5.4), and the architectural patterns that emerge from Fisher-based selection across model families (Section 5.5).

5.1 Why Layer Reduction Beats Rank Reduction

Alternatively, halving the rank across all layers preserves coverage but halves each adapter’s subspace dimension, reducing expressiveness. Conversely, FoRA preserves per-adapter rank and reduces the number of adapted layers while keeping the per-adapter rank intact. Both strategies arrive at the same trainable parameter count, so they form a controlled comparison along the parameter axis. We test both on LLaMA-3.2-3B at the matched budget $P_0/2$, where P_0 is the parameter count of vanilla LoRA at $r = 32$ on all layers. Table 5 reports the commonsense reasoning average for four configurations: the full LoRA baseline at P_0 , one budget- $P_0/2$ configuration from the rank-reduction family (LoRA at $r = 16$ on all layers), and the budget- $P_0/2$ configurations from the layer-reduction family (FG-LoRA and FoRA).

At the matched $P_0/2$ budget, rank reduction (LoRA $r=16$, PPL 7.35) and Fisher-top- K selection (FG-LoRA, 7.38) are within seed noise of each

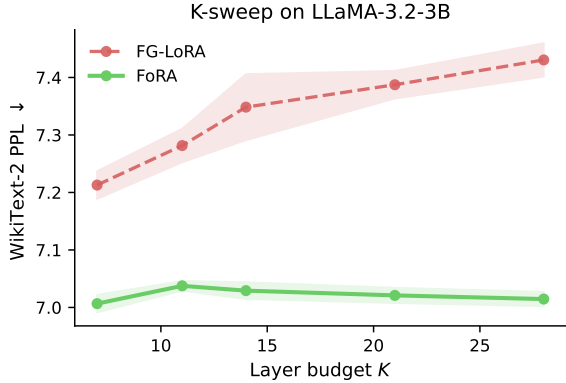


Figure 2: Sensitivity to layer budget K on LLaMA-3.2-3B with $n_{\text{train}} = 4096$, three seeds. FoRA is essentially flat across $K \in \{7, 11, 14, 21, 28\}$.

other: without a structural constraint, *where* parameters go and *how* the rank is cut are roughly interchangeable. The decisive gain comes from the Stiefel constraint: adding it to Fisher-top- K (FoRA) drops PPL by an additional 0.35, well outside the seed-noise band. Layer reduction is not the source of the win by itself; it becomes effective precisely when each remaining adapter is forced to use its rank in full.

5.2 Sensitivity to Layer Budget K

A natural concern is whether the choice $K = L/2$ used throughout Section 4 is a tunable hyperparameter that drives the reported gains. We examine this by sweeping K from $L/4$ to L on LLaMA-3.2-3B and comparing FG-LoRA (Fisher selection only) with FoRA. Figure 2 shows the result. FG-LoRA degrades monotonically as K grows beyond the Fisher-selected core, indicating that adding non-informative layers consumes parameters without yielding accuracy. In contrast, FoRA is essentially flat across the entire K range, with variation within the seed standard deviation. Two conclusions follow. First, the layer budget K is not a sensitive hyperparameter for FoRA, so the choice of $K = L/2$ in Sections 4.2, 4.3, 4.4 is a defensible default rather than a tuned cherry-pick. Second, the Stiefel constraint absorbs the cost of including non-informative layers, which is a desirable property when the optimal layer budget is unknown a priori. Appendix H replicates this analysis on Gemma-3-1B-pt and confirms the same qualitative pattern holds across model families.

Method	erank	ratio	$\ \Delta W\ _F$	KL
LoRA-all	22.84	0.71	9.2	0.160
FG-LoRA	21.80	0.68	7.3	0.128
Stiefel-LoRA	28.77	0.90	95.9	0.054
FoRA (Ours)	28.07	0.88	80.6	0.053

Table 6: The Stiefel-constrained methods (FoRA and Stiefel-LoRA) recover effective rank to 0.88–0.90 r and make $\sim 10\times$ larger weight changes than unconstrained methods, yet shift the output distribution $\sim 3\times$ less. LLaMA-3.2-3B, seed 42, $n_{\text{train}} = 4096$, $r = 32$.

5.3 Stiefel Mechanism: Rank Preservation and Orthogonal Updates

Section 3 argued via a small lemma that the Stiefel constraint preserves the effective rank of $\Delta W = BA$ at $\text{rank}(A)$. We verify this empirically by measuring the effective rank of trained adapters under bf16 mixed precision. Following Roy and Vetterli (2007), we report the entropy-based effective rank $\text{erank}(M) = \exp(H(\sigma_i / \sum_j \sigma_j))$ where $\{\sigma_i\}$ are the singular values of $M = BA$ and H is the Shannon entropy. Table 6 reports mean effective rank, weight-change magnitude $\|\Delta W\|_F$, and output drift $\text{KL}(p_{\text{trained}} \| p_{\text{base}})$ across four configurations on LLaMA-3.2-3B with $r = 32$.

Unconstrained adapters (LoRA-all, FG-LoRA) converge to effective rank 0.68–0.71 of $r = 32$, replicating the spectral collapse of Biderman et al. (2024); Hayou et al. (2024); the collapse is worse in FG-LoRA, where each remaining adapter must compress more task signal. Stiefel-constrained methods (FoRA, Stiefel-LoRA) recover effective rank to 0.88–0.90 of r , confirming Lemma 1 under mixed-precision training: Stiefel adapters maintain a near-flat singular-value plateau across all r directions before dropping sharply at index r , while unconstrained adapters decay rapidly from the first singular value. Appendix H replicates this pattern on Qwen3-4B and Gemma-3-1B-pt across all four target module types.

A third observation reconciles two apparently contradictory facts in Table 6. The Stiefel-constrained methods achieve their effective-rank recovery by making much larger weight changes ($\|\Delta W\|_F$ 80–96) than the unconstrained methods ($\|\Delta W\|_F$ 7–9), yet their output distributions stay closer to the base model (KL 0.053–0.054 vs. 0.128–0.160). The explanation is structural: a column-orthonormal B maps \mathbb{R}^r into a flat r -dimensional subspace of the output space, so the additional Frobenius mass in ΔW is spread uniformly across r orthogonal directions rather than

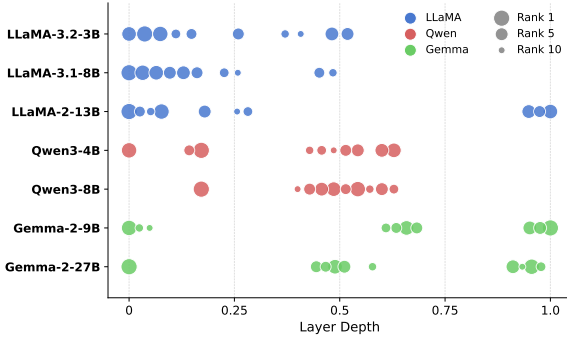


Figure 3: Fisher-selected top-10 layer indices for seven backbones. Layer depth is normalized (0 = first, 1 = last); dot size encodes rank within the top-10.

concentrated on a few dominant ones. This explains the super-additivity of FoRA: the Stiefel constraint matters most exactly where the rank deficit is largest, i.e., in the selective setting where each remaining adapter must use its full rank.

5.4 Why Diagonal Fisher Suffices

The Fisher score we use in Section 3 aggregates the squared gradients of the base parameters within each layer, treating different layers as independent blocks. A natural question is whether this block-diagonal approximation discards important cross-layer interactions and therefore mis-ranks the layers. We measure the cross-layer gradient correlation on LLaMA-3.2-3B over 64 mini-batches. Off-diagonal entries have mean magnitude 0.0035 and maximum 0.047 (off/on ratio 0.35%), so the per-layer FIM is nearly block-diagonal and the diagonal approximation retains the ranking signal. We further compare three Fisher estimation strategies (diagonal, K-FAC (Martens and Grosse, 2015), and true Fisher) on LLaMA-3.2-3B. Diagonal and K-FAC agree exactly on the top-8 layers (Jaccard 1.0), and the PPL difference between diagonal and true Fisher (8.47 vs. 8.35) is small relative to the $3\times$ reduction in scoring time and 30% memory saving over K-FAC. Full results are in Appendix D.

5.5 Architectural Patterns of Selected Layers

A second-order question is whether Fisher selection produces architecturally interpretable patterns or simply scatters across layers. We extract the top- K Fisher-selected layers from each model in our cross-architecture study and compare the index distributions. Figure 3 summarizes the result. The three model families exhibit qualitatively different selection patterns. The LLaMA family concen-

trates Fisher mass in the initial layers; specifically, top-10 selections for LLaMA-3.2-1B, LLaMA-3.2-3B, and LLaMA-3.1-8B all place layers 0, 1, 2 in the top three positions, with the remainder drawn from the lower-middle stack. The Qwen3 family shifts selections toward the middle of the stack: Qwen3-8B places layers 14, 15, 16 at the top, with no early layer in the top three. The Gemma-2 family at larger scale concentrates selections at the top of the stack: Gemma-2-9B places layers 39, 40, 41 alongside layer 0, indicating a bimodal pattern with both very early and very late layers carrying high task-relevant Fisher mass.

These family-specific patterns argue against any fixed layer schedule (e.g., “always adapt the first K layers”): such a schedule fits LLaMA but not Qwen or Gemma. They also suggest that Fisher-selected layers reflect per-model information concentration from pretraining rather than a universal transformer property, motivating architecture-aware PEFT design.

6 Conclusion

We present FoRA, a parameter-efficient fine-tuning method that integrates Fisher-based layer selection with a Stiefel-manifold constraint on the LoRA adaptation matrices. By concentrating the adaptation budget on the layers most informative to the target task, identified via a single forward-backward pass costing less than 1% of training, and enforcing column-orthonormality of the B matrix via Cayley-Adam, FoRA achieves strong performance at roughly half the parameter count of standard LoRA.

Empirically, FoRA consistently outperforms LoRA and DoRA on a seven-task commonsense benchmark across five LLaMA-family backbones while using approximately half their trainable parameters. Against AdaLoRA, which requires twice the parameter budget of LoRA, FoRA falls within 0.7–0.8 accuracy points on four of five models at one-quarter its parameter count, establishing a favorable efficiency frontier that neither LoRA nor AdaLoRA occupies. The method generalizes across 12 backbone architectures spanning the LLaMA, Qwen3, and Gemma families at scales from 270M to 32B parameters. Ablation and diagnostic studies confirm that the two components are complementary: Fisher-based layer selection concentrates the parameter budget on task-informative layers, and the Stiefel constraint

restores effective rank utilization from 0.71 to 0.88 of the nominal rank, with the two combining super-additively. Architecture-specific Fisher profiles, including early-stack concentration in LLaMA, middle-stack in Qwen3, and bimodal early-plus-late in Gemma, suggest that Fisher-guided selection captures genuine structural differences across model families, opening a direction toward architecture-aware PEFT design.

Limitation

FoRA achieves parameter-efficient fine-tuning with strong empirical performance, but several limitations remain. The Fisher-based layer selection relies on a single forward-backward pass over a fixed calibration set and does not adapt during training, which may reduce effectiveness when the calibration distribution diverges from the target task. Although holding the selection \mathcal{S} static prevents the model from adapting to shifting layer importance during late-stage training, this static choice completely eliminates the massive, step-wise SVD computation overhead incurred by dynamic allocation methods like AdaLoRA, establishing a highly practical efficiency-accuracy frontier. The Cayley-Adam retraction introduces approximately 10–15% additional wall-clock training time per step relative to standard LoRA; for very large models, this overhead can partially offset the efficiency gained from reducing the number of adapted layers, though truncated fixed-point approximations of the Cayley transform can mitigate this cost in practice. Additionally, on LLaMA-3.2-1B, FoRA falls slightly below AdaLoRA in average accuracy (57.4 vs. 58.1) despite using one-quarter of AdaLoRA’s parameter budget, suggesting that aggressive layer pruning becomes less reliable when per-layer capacity is severely constrained. These trade-offs notwithstanding, FoRA consistently matches or outperforms LoRA-family baselines across larger backbones and multiple model families, demonstrating that its design choices are well-suited to the practical regimes where parameter efficiency matters most.

References

Shun-ichi Amari. 1998. Natural gradient works efficiently in learning. *Neural Computation*, 10(2):251–276.

Dan Biderman, Jacob Portes, Jose Javier Gonzalez Ortiz, Mansheej Paul, Philip Greengard, Connor Jennings,

Daniel King, Sam Havens, Vitaliy Chiley, Jonathan Frankle, Cody Blakeney, and John P. Cunningham. 2024. LoRA learns less and forgets less. *TMLR*.

Yonatan Bisk, Rowan Zellers, Ronan Le bras, Jianfeng Gao, and Yejin Choi. 2020. PIQA: Reasoning about physical commonsense in natural language. In *AAAI*.

Christopher Clark, Kenton Lee, Ming-Wei Chang, Tom Kwiatkowski, Michael Collins, and Kristina Toutanova. 2019. BoolQ: Exploring the surprising difficulty of natural yes/no questions. In *NAACL*.

Peter Clark, Isaac Cowhey, Oren Etzioni, Tushar Khot, Ashish Sabharwal, Carissa Schoenick, and Oyvind Tafjord. 2018. Think you have solved question answering? try ARC, the AI2 reasoning challenge. *arXiv preprint arXiv:1803.05457*.

Tim Dettmers, Artidoro Pagnoni, Ari Holtzman, and Luke Zettlemoyer. 2023. QLoRA: Efficient finetuning of quantized LLMs. In *NeurIPS*.

Soufiane Hayou, Nikhil Ghosh, and Bin Yu. 2024. LoRA+: Efficient low rank adaptation of large models.

Edward J. Hu, Yelong Shen, Phillip Wallis, Zeyuan Allen-Zhu, Yuanzhi Li, Shean Wang, Lu Wang, and Weizhu Chen. 2022. LoRA: Low-rank adaptation of large language models. In *ICLR*.

Zhiqiang Hu, Lei Wang, Yihuai Lan, Wanyu Xu, Ee-Peng Lim, Lidong Bing, Xing Xu, Soujanya Poria, and Roy Ka-Wei Lee. 2023. LLM-adapters: An adapter family for parameter-efficient fine-tuning of large language models. *EMNLP*.

Damjan Kalajdzievski. 2023. A rank stabilization scaling factor for fine-tuning with LoRA. *arXiv preprint arXiv:2312.03732*.

Dawid Jan Kopiczko, Tijmen Blankevoort, and Yuki M. Asano. 2024. VeRA: Vector-based random matrix adaptation. In *ICLR*.

Frederik Kunstner, Lukas Balles, and Philipp Hennig. 2019. Limitations of the empirical Fisher approximation for natural gradient descent. In *NeurIPS*.

Shih-Yang Liu, Chien-Yi Wang, Hongxu Yin, Pavlo Molchanov, Yu-Chiang Frank Wang, Kwang-Ting Cheng, and Min-Hung Chen. 2024a. DoRA: Weight-decomposed low-rank adaptation. In *ICML*.

Weiyang Liu, Zeju Qiu, Yao Feng, Yuliang Xiu, Yuxuan Xue, Longhui Yu, Haiwen Feng, Zhen Liu, Juyeon Heo, Songyou Peng, Yandong Wen, Michael J. Black, Adrian Weller, and Bernhard Schölkopf. 2024b. Parameter-efficient orthogonal finetuning via butterfly factorization. In *ICLR*.

James Martens and Roger Grosse. 2015. Optimizing neural networks with Kronecker-factored approximate curvature. In *ICML*.

- Fanxu Meng, Zhaohui Wang, and Muhan Zhang. 2024. PiSSA: Principal singular values and singular vectors adaptation of large language models. *NeurIPS*.
- Stephen Merity, Caiming Xiong, James Bradbury, and Richard Socher. 2017. Pointer sentinel mixture models. In *ICLR*.
- Todor Mihaylov, Peter Clark, Tushar Khot, and Ashish Sabharwal. 2018. Can a suit of armor conduct electricity? a new dataset for open book question answering. In *EMNLP*.
- Rui Pan, Xiang Liu, Shizhe Diao, Renjie Pi, Jipeng Zhang, Chi Han, and Tong Zhang. 2024. LISA: Layerwise importance sampling for memory-efficient large language model fine-tuning. *NeurIPS*.
- JuneYoung Park, Minjae Kang, Seongbae Lee, Haegang Lee, Seongwan Kim, and Jaeho Lee. 2025. [Riemannian optimization for LoRA on the Stiefel manifold](#). In *Findings of the Association for Computational Linguistics: EMNLP 2025*, pages 20971–20985, Suzhou, China. Association for Computational Linguistics.
- Zeju Qiu, Weiyang Liu, Haiwen Feng, Yuxuan Xue, Yao Feng, Zhen Liu, Dan Zhang, Adrian Weller, and Bernhard Schölkopf. 2023. Controlling text-to-image diffusion by orthogonal finetuning. In *NeurIPS*.
- Olivier Roy and Martin Vetterli. 2007. The effective rank: A measure of effective dimensionality. *EU-SIPCO*.
- Keisuke Sakaguchi, Ronan Le Bras, Chandra Bhagavatula, and Yejin Choi. 2020. WinoGrande: An adversarial Winograd schema challenge at scale. *Communications of the ACM*.
- Rohan Taori, Ishaan Gulrajani, Tianyi Zhang, Yann Dubois, Xuechen Li, Carlos Guestrin, Percy Liang, and Tatsunori B. Hashimoto. 2023. Stanford Alpaca: An instruction-following LLaMA model. https://github.com/tatsu-lab/stanford_alpaca.
- Zaiwen Wen and Wotao Yin. 2013. A feasible method for optimization with orthogonality constraints. *Mathematical Programming*, 142(1):397–434.
- Rowan Zellers, Ari Holtzman, Yonatan Bisk, Ali Farhadi, and Yejin Choi. 2019. HellaSwag: Can a machine really finish your sentence? In *ACL*.
- Qingru Zhang, Minshuo Chen, Alexander Bukharin, Pengcheng He, Yu Cheng, Weizhu Chen, and Tuo Zhao. 2023. AdaLoRA: Adaptive budget allocation for parameter-efficient fine-tuning. In *ICLR*.
- Lianmin Zheng, Wei-Lin Chiang, Ying Sheng, Siyuan Zhuang, Zhanghao Wu, Yonghao Zhuang, Zi Lin, Zhuohan Li, Dacheng Li, Eric P. Xing, Hao Zhang, Joseph E. Gonzalez, and Ion Stoica. 2023. Judging LLM-as-a-judge with MT-Bench and chatbot arena. In *NeurIPS Datasets and Benchmarks Track*.
- Hongyun Zhou, Xiangyu Lu, Wang Xu, Conghui Zhu, Tiejun Zhao, and Muyun Yang. 2024. LoRA-drop: Efficient LoRA parameter pruning based on output evaluation. *arXiv preprint arXiv:2402.07721*.

A FoRA Training Algorithm

Algorithm 1 gives the full training procedure for FoRA. The procedure has two phases. Phase 1 computes the empirical diagonal Fisher score for every layer using N mini-batches of the task data with the frozen base model, and selects the top- K layers. Phase 2 inserts LoRA adapters at the selected layers, attaches a Cayley-Adam optimizer to the down-projection B_ℓ and an AdamW optimizer to the up-projection A_ℓ , and runs joint training. The two optimizers are stepped together at every iteration. Periodic QR re-projection on B_ℓ is included to control numerical drift in mixed precision; in practice we apply it every T_{qr} steps with $T_{\text{qr}} = 200$.

Algorithm 1 FoRA training procedure.

Require: pretrained model θ_0 with L layers, dataset \mathcal{D} , rank r , top- K , Fisher batches N , Cayley iterations n_c , QR period T_{qr} , learning rates α_A, α_B

Phase 1: Fisher-based layer selection

- 1: $F_\ell \leftarrow 0$ for all $\ell \in \{1, \dots, L\}$
- 2: **for** $n = 1$ to N **do**
- 3: sample mini-batch $(x_n, y_n) \sim \mathcal{D}$
- 4: compute $g_n \leftarrow \nabla_{\theta_0} \mathcal{L}(x_n, y_n)$
- 5: **for** each layer ℓ **do**
- 6: $F_\ell \leftarrow F_\ell + \sum_{\theta \in \theta_\ell^{\text{base}}} \|g_{n, \theta}\|^2$
- 7: **end for**
- 8: **end for**
- 9: $F_\ell \leftarrow F_\ell / N$ for all ℓ
- 10: $\mathcal{S} \leftarrow \text{TopK}(\{F_\ell\}, K)$

Phase 2: dual-optimizer training

- 11: **for** each $\ell \in \mathcal{S}$, initialize $A_\ell \sim \mathcal{N}(0, \sigma^2)$ and $B_\ell \leftarrow \text{QR}(G)$ where $G \in \mathbb{R}^{d_{\text{out}} \times r}$ has i.i.d. standard normal entries (random orthonormal columns); $\Delta W_\ell = B_\ell A_\ell$ is small at $t = 0$ due to the scaling $\sigma = 1/\sqrt{r}$
 - 12: attach AdamW(α_A) to $\{A_\ell\}_{\ell \in \mathcal{S}}$ and CayleyAdam(α_B, n_c) to $\{B_\ell\}_{\ell \in \mathcal{S}}$
 - 13: **for** $t = 1$ to T_{train} **do**
 - 14: sample mini-batch from \mathcal{D} , compute loss \mathcal{L}_t
 - 15: backpropagate to update Adam moments for A_ℓ and B_ℓ
 - 16: step AdamW on $\{A_\ell\}$ ▷ standard Euclidean update
 - 17: step CayleyAdam on $\{B_\ell\}$ ▷ Eq. (6), n_c inner iterations
 - 18: **if** $t \bmod T_{\text{qr}} = 0$ **then**
 - 19: re-project $B_\ell \leftarrow \text{QR}(B_\ell)$ for all $\ell \in \mathcal{S}$
 - 20: **end if**
 - 21: **end for**
 - 22: **return** adapted model with $\Delta W_\ell = B_\ell A_\ell$ for $\ell \in \mathcal{S}$
-

B Per-task Cross-architecture Results

Table 7 reports the per-task accuracy for the cross-architecture comparison summarized by Table 2. LLaMA-3.2-3B was evaluated on the four tasks shared across all backbones (PIQA, HellaSwag, WinoGrande, ARC-easy); the remaining backbones additionally report BoolQ, ARC-challenge, and OpenBookQA. Cell entries are mean over three seeds (four seeds for LLaMA-3.2-3B).

Model	Method	Fisher	Stiefel	Params (M)	BoolQ	PIQA	HellaS	WinoG	ARC-e	ARC-c	OBQA	CS-Avg
<i>Gemma family</i>												
Gemma-3-270M	LoRA-all	✗	✗	5.1	56.4	67.3	39.0	52.9	53.5	26.8	31.6	53.16
	FG-LoRA	✓	✗	2.5	59.8	66.3	39.4	52.8	51.9	27.1	31.6	52.61
	Stiefel-LoRA	✗	✓	5.1	59.7	66.5	38.0	52.8	48.3	25.6	29.9	51.39
	FoRA (Ours)	✓	✓	2.5	59.5	66.3	39.2	54.5	51.4	25.9	30.7	52.85
Gemma-3-1B	LoRA-all	✗	✗	17.6	60.8	73.7	58.6	56.7	61.7	34.3	38.8	62.69
	FG-LoRA	✓	✗	8.8	62.9	73.7	59.4	57.4	62.3	33.3	39.3	63.19
	Stiefel-LoRA	✗	✓	17.6	62.4	74.2	58.4	59.2	65.4	34.5	36.9	64.31
	FoRA (Ours)	✓	✓	8.8	61.6	74.5	59.9	59.2	68.6	36.4	37.7	65.55
Gemma-2-9B	LoRA-all	✗	✗	73.6	81.7	78.6	71.7	68.9	60.4	40.6	46.8	69.90
	FG-LoRA	✓	✗	36.8	80.1	80.4	76.0	71.7	72.6	50.4	47.2	75.15
	Stiefel-LoRA	✗	✓	73.6	85.1	83.2	79.5	77.7	84.7	61.3	44.6	81.29
	FoRA (Ours)	✓	✓	36.8	84.6	82.3	79.0	75.9	85.4	62.8	44.6	80.66
Gemma-2-27B	LoRA-all	✗	✗	154.5	83.3	79.9	78.3	72.8	58.1	37.8	47.0	72.28
	FG-LoRA	✓	✗	77.3	83.5	82.3	79.5	73.2	65.7	43.9	49.6	75.18
	Stiefel-LoRA	✗	✓	154.5	82.0	83.5	82.1	76.4	83.7	60.2	46.5	81.44
	FoRA (Ours)	✓	✓	77.3	81.1	84.3	84.0	78.7	87.8	65.9	47.4	83.68
<i>Qwen family</i>												
Qwen3-0.6B	LoRA-all	✗	✗	13.8	68.7	70.3	51.5	57.1	59.7	36.0	36.8	59.64
	FG-LoRA	✓	✗	6.9	66.1	69.7	52.1	56.1	59.2	35.2	35.7	59.28
	Stiefel-LoRA	✗	✓	13.8	65.6	70.0	50.3	59.0	61.3	35.9	35.9	60.16
	FoRA (Ours)	✓	✓	6.9	54.1	69.9	51.6	58.7	59.0	35.6	34.4	59.81
Qwen3-1.7B	LoRA-all	✗	✗	23.9	75.9	72.7	62.3	60.3	58.9	36.7	41.8	63.55
	FG-LoRA	✓	✗	11.9	75.8	73.7	61.8	60.9	60.2	37.6	38.9	64.14
	Stiefel-LoRA	✗	✓	23.9	71.8	72.5	61.5	63.8	61.2	36.6	39.9	64.75
	FoRA (Ours)	✓	✓	11.9	76.1	73.0	61.2	62.2	66.8	39.9	37.5	65.80
Qwen3-4B	LoRA-all	✗	✗	44.2	83.0	75.6	70.1	63.8	60.6	39.2	42.6	67.52
	FG-LoRA	✓	✗	22.1	83.2	75.4	69.8	65.6	60.5	39.2	42.6	67.84
	Stiefel-LoRA	✗	✓	44.2	82.2	77.3	70.9	66.3	74.8	48.6	42.4	72.30
	FoRA (Ours)	✓	✓	22.1	84.0	76.9	70.5	69.8	65.6	44.4	40.0	70.69
Qwen3-8B	LoRA-all	✗	✗	59.0	83.6	78.0	74.4	67.2	57.6	39.5	41.2	69.31
	FG-LoRA	✓	✗	29.5	83.9	78.2	75.9	67.8	60.4	40.1	44.4	70.57
	Stiefel-LoRA	✗	✓	59.0	82.5	78.8	76.5	69.9	66.9	45.6	40.8	73.04
	FoRA (Ours)	✓	✓	29.5	85.6	78.8	76.7	70.2	74.2	48.3	42.0	74.98
Qwen3-32B	LoRA-all	✗	✗	178.3	88.6	80.3	79.1	67.9	67.3	45.6	47.4	73.65
	FG-LoRA	✓	✗	89.1	88.5	80.4	80.8	69.1	59.3	42.5	46.8	72.40
	Stiefel-LoRA	✗	✓	178.3	78.7	80.8	81.8	70.6	73.8	52.5	45.6	76.76
	FoRA (Ours)	✓	✓	89.1	84.5	81.2	82.2	72.3	74.4	52.6	44.6	77.51
<i>LLaMA family</i>												
LLaMA-3.2-3B	LoRA-all	✗	✗	33.0	76.2	76.1	71.3	65.3	62.7	36.5	41.2	68.86
	FG-LoRA	✓	✗	16.5	76.8	76.6	72.7	67.0	62.5	37.8	41.5	69.70
	Stiefel-LoRA	✗	✓	33.0	78.4	77.3	71.4	69.0	67.3	40.2	42.0	71.26
	FoRA (Ours)	✓	✓	16.5	79.0	77.5	72.5	70.5	68.1	41.6	41.8	72.18
LLaMA-3.1-8B	LoRA-all	✗	✗	56.6	81.2	79.3	74.0	69.9	59.1	40.1	44.6	70.54
	FG-LoRA	✓	✗	28.3	81.5	80.3	77.5	71.7	67.3	44.0	45.0	74.21
	Stiefel-LoRA	✗	✓	56.6	83.0	81.2	77.5	75.1	69.0	44.2	45.6	75.67
	FoRA (Ours)	✓	✓	28.3	82.7	81.6	78.6	76.6	76.1	47.7	45.4	78.21
LLaMA-2-13B	LoRA-all	✗	✗	87.8	79.3	78.9	75.8	69.3	59.5	39.0	46.6	70.86
	FG-LoRA	✓	✗	43.9	77.7	79.2	78.2	70.8	62.0	39.9	48.0	72.56
	Stiefel-LoRA	✗	✓	87.8	83.3	80.6	78.1	74.7	76.5	49.5	46.2	77.49
	FoRA (Ours)	✓	✓	43.9	82.6	80.6	79.3	74.1	74.3	47.8	46.8	77.08

Table 7: Full per-task accuracy for the cross-architecture comparison summarized by Table 2 in the main text. Models are grouped by family. Mean over available seeds (single seed for the largest backbones; three to four seeds for the smaller ones). *CS-Avg* denotes the mean accuracy over the four commonsense tasks shared by every backbone (PIQA, HellaSwag, WinoGrande, ARC-easy).

C Stiefel Optimization Details

This appendix collects the technical material that supports the Stiefel update used by FoRA: a proof of Lemma 1, the derivation of the Cayley parametrization and its orthogonality-preserving property, the fixed-point iteration we use to apply the update without forming a $d_{\text{out}} \times d_{\text{out}}$ matrix inverse, and the periodic QR re-projection that keeps the constraint satisfied under bf16 mixed precision.

Proof of Lemma 1 (singular value preservation). Let $A = U_A \Sigma_A V_A^\top$ be a thin singular value decomposition with $U_A \in \mathbb{R}^{r \times r}$ orthogonal, $\Sigma_A \in \mathbb{R}^{r \times r}$ diagonal with non-negative entries, and $V_A \in \mathbb{R}^{d_{\text{in}} \times r}$ with orthonormal columns. Define $Q = B U_A \in \mathbb{R}^{d_{\text{out}} \times r}$. Then

$$Q^\top Q = U_A^\top B^\top B U_A = U_A^\top I_r U_A = I_r,$$

since $B \in \text{St}(d_{\text{out}}, r)$ implies $B^\top B = I_r$ and U_A is orthogonal. Therefore $BA = Q \Sigma_A V_A^\top$ is a thin SVD-like factorization with Q having orthonormal columns and V_A having orthonormal columns, and Σ_A on the diagonal. The non-zero singular values of BA are exactly the diagonal entries of Σ_A , which are the singular values of A . \square

Riemannian gradient on the Stiefel manifold. For $B \in \text{St}(d_{\text{out}}, r)$, the tangent space $T_B \text{St}$ consists of matrices $\xi \in \mathbb{R}^{d_{\text{out}} \times r}$ satisfying $B^\top \xi + \xi^\top B = 0$. The Euclidean gradient $G = \partial \mathcal{L} / \partial B$ is projected onto $T_B \text{St}$ by

$$\text{grad}_B \mathcal{L} = G - B \text{sym}(B^\top G), \quad \text{sym}(M) := \frac{1}{2}(M + M^\top). \quad (7)$$

Equivalently, this projection can be written as left-multiplication by a skew-symmetric matrix on B :

$$\text{grad}_B \mathcal{L} = (\widehat{W} - \widehat{W}^\top) B, \quad \widehat{W} = G B^\top - \frac{1}{2} B B^\top G B^\top, \quad (8)$$

which is the form used in Eq. (5) of the main text. We use Eq. (8) because it isolates the geometry into a single skew-symmetric matrix $W = \widehat{W} - \widehat{W}^\top$ that drives the Cayley transform below.

Cayley transform preserves orthogonality. For any skew-symmetric matrix $W = -W^\top$ and any step size α , the Cayley transform

$$Q(W, \alpha) := (I - \frac{\alpha}{2} W)^{-1} (I + \frac{\alpha}{2} W)$$

is orthogonal whenever the inverse exists. Indeed,

$$\begin{aligned} Q^\top Q &= (I + \frac{\alpha}{2} W)^\top (I - \frac{\alpha}{2} W)^{-\top} (I - \frac{\alpha}{2} W)^{-1} (I + \frac{\alpha}{2} W) \\ &= (I - \frac{\alpha}{2} W) (I + \frac{\alpha}{2} W)^{-1} (I - \frac{\alpha}{2} W)^{-1} (I + \frac{\alpha}{2} W), \end{aligned}$$

where we used $W^\top = -W$ so that $(I + \frac{\alpha}{2} W)^\top = I - \frac{\alpha}{2} W$ and similarly for the other factor. Since $(I - \frac{\alpha}{2} W)$ and $(I + \frac{\alpha}{2} W)$ commute, the product simplifies to I . Therefore the update $B^{(t+1)} = Q(W, \alpha) B^{(t)}$ preserves $B^\top B = I_r$ exactly in real arithmetic.

Fixed-point iteration without forming the inverse. A direct evaluation of Eq. (6) would require inverting $(I - \frac{\alpha}{2} W) \in \mathbb{R}^{d_{\text{out}} \times d_{\text{out}}}$, which is prohibitive for hidden sizes of several thousand. We avoid this by recognizing that Eq. (6) is equivalent to the linear equation

$$Y = B^{(t)} + \frac{\alpha}{2} W (B^{(t)} + Y), \quad (9)$$

which we solve by the simple fixed-point iteration $Y^{(0)} = B^{(t)} + \alpha W B^{(t)}$, $Y^{(k+1)} = B^{(t)} + \frac{\alpha}{2} W (B^{(t)} + Y^{(k)})$ for $k = 0, 1, \dots, n_c - 1$. Each iteration costs a single matrix product WX with $W \in \mathbb{R}^{d_{\text{out}} \times d_{\text{out}}}$ and $X \in \mathbb{R}^{d_{\text{out}} \times r}$, but in practice we do not materialize W . Since $W = \widehat{W} - \widehat{W}^\top$ with $\widehat{W} = G B^\top - \frac{1}{2} B B^\top G B^\top$ has rank at most $2r$, we form WX as a sequence of $(d_{\text{out}} \times r)$ -shaped tensor contractions in $\mathcal{O}(d_{\text{out}} r^2)$ work per multiplication. The total cost of the inner solve is therefore $\mathcal{O}(n_c d_{\text{out}} r^2)$ per optimizer step, which is dominated by the $\mathcal{O}(d_{\text{out}} d_{\text{in}} r)$ cost of the LoRA forward and backward passes for $r \ll d_{\text{in}}$.

Adam moments on the manifold. The skew direction W in Eq. (5) replaces the raw Euclidean gradient with the first-moment estimate \widehat{m} of Adam, and the step size α is divided by the square root of a scalar second-moment estimate \widehat{v} derived from the Frobenius norm of the gradient. This produces a Cayley-Adam update of the form

$$B^{(t+1)} = Q\left(\frac{\widehat{W}_m - \widehat{W}_m^\top}{\sqrt{\widehat{v} + \epsilon}}, \alpha\right) B^{(t)},$$

where \widehat{W}_m is constructed from \widehat{m} via Eq. (8). Bias correction and momentum decay schedules follow Adam exactly.

Periodic QR re-projection. In real arithmetic the Cayley transform preserves orthogonality exactly, but bf16 arithmetic accumulates rounding error so that $\|B^\top B - I_r\|_F$ slowly grows during training. We control this drift by re-projecting B to $St(d_{\text{out}}, r)$ every T_{qr} optimizer steps via the QR retraction $B \leftarrow Q$, where $B = QR$ is the thin QR factorization with R chosen to have non-negative diagonal entries. We use $T_{\text{qr}} = 200$ in all experiments; we measured the Frobenius drift to remain below 10^{-3} over 10^4 steps with this schedule on LLaMA-3.2-3B in bf16.

Cost summary. The end-to-end per-step cost of the FoRA optimizer is therefore

$$\underbrace{\mathcal{O}(d_{\text{out}}d_{\text{in}}r)}_{\text{LoRA forward+backward}} + \underbrace{\mathcal{O}(n_c d_{\text{out}}r^2)}_{\text{Cayley fixed-point}} + \underbrace{\mathcal{O}(d_{\text{out}}r^2/T_{\text{qr}})}_{\text{amortized QR}}$$

which is asymptotically the same as standard LoRA whenever $r \ll d_{\text{in}}$ and n_c is held constant, matching the empirical wall-clock observation that FoRA training time is within 10–15% of the corresponding LoRA-all run on LLaMA-3.2-3B.

D Fisher Score Approximation: Diagonal vs. K-FAC vs. True Fisher

Table 8 compares three strategies for computing the layer-wise Fisher score on LLaMA-3.2-3B: our diagonal empirical Fisher (squared gradient norms), K-FAC (Martens and Grosse, 2015), and the true Fisher (using model-sampled rather than ground-truth labels). We evaluate each strategy on (i) the WikiText-2 perplexity after fine-tuning with the selected $K=L/2$ layers, (ii) the wall-clock time to score all layers over $N=128$ mini-batches, (iii) peak GPU memory during scoring, and (iv) layer-ranking agreement with the diagonal approximation measured by the Jaccard index of the top-8 selected layers ($J@8$) and Kendall’s τ .

Strategy	PPL	Time (s)	Mem (GB)	J@8	τ
Diagonal (Ours)	8.47	29.3	14.9	1.00	–
K-FAC	8.46	36.8	21.2	1.00	0.43
True Fisher	8.35	87.7	15.4	0.33	0.53

Table 8: Comparison of Fisher score estimation strategies on LLaMA-3.2-3B ($N=128$ mini-batches, $K=L/2$, single H200). **PPL**: WikiText-2 perplexity of the fine-tuned model using the selected layers. **J@8**: Jaccard index of top-8 selected layers relative to the diagonal strategy. τ : Kendall’s τ layer-rank correlation with the diagonal strategy. The diagonal approximation matches K-FAC’s top-8 selection exactly ($J@8 = 1.0$) at lower computational cost, and trades a 0.12 PPL gap for a $3\times$ reduction in scoring time relative to true Fisher.

E Training Efficiency: Memory and Throughput

Table 9 reports peak GPU memory, training throughput, and per-step latency for three configurations on LLaMA-3.2-3B: a frozen baseline (no adapters), LoRA-all (all L layers adapted), and FG-LoRA (Fisher-selected top $K=L/2$ layers). All measurements use batch size 16, sequence length 256, and bf16 precision on a single NVIDIA H200. FoRA uses the same layer selection as FG-LoRA and therefore has an identical memory footprint; the Stiefel update adds a per-step overhead that keeps total FoRA training time within 10–15% of LoRA-all (see Appendix C, Cost summary).

Method	Peak Mem (GB)	Throughput (tok/s)	Step (ms)
Frozen baseline	32.96	9,621	105.9
LoRA-all	15.32	10,442	97.5
FG-LoRA / FoRA	12.45	15,210	67.1

Table 9: Training efficiency on LLaMA-3.2-3B (batch size 16, sequence length 256, bf16, single H200). Per-step latency is decomposed as forward 29.6 ms + backward 35.7 ms + optimizer 1.8 ms for FG-LoRA/FoRA vs. forward 42.7 ms + backward 50.5 ms + optimizer 4.3 ms for LoRA-all. Selecting half of the layers reduces peak memory by 19% and improves throughput by 46% relative to LoRA-all; FoRA’s Stiefel update adds ~ 10 –15% wall-clock overhead over FG-LoRA on this backbone.

F Hyperparameters

Table 10 lists the hyperparameters used in this paper for every method whose results we report. Common training settings are $r = 32$, $\alpha = 64$, batch size 16, gradient accumulation 4, weight decay 0.01, AdamW $\beta_1 = 0.9$, $\beta_2 = 0.999$, three training epochs over the full Commonsense-170K corpus, target modules $\{q, k, v, \text{up}, \text{down}\}$, sequence length 256, and bf16 mixed-precision training. Method-specific hyperparameters are summarized below.

Method	α_A	α_B	dropout	K	N	n_c	T_{qr}
LoRA-all	$2 \cdot 10^{-4}$	–	0.05	L	–	–	–
FG-LoRA	$2 \cdot 10^{-4}$	–	0.05	$L/2$	128	–	–
Stiefel-LoRA	$2 \cdot 10^{-4}$	$1 \cdot 10^{-3}$	–	L	–	5	200
FoRA (Ours)	$2 \cdot 10^{-4}$	$1 \cdot 10^{-3}$	–	$L/2$	128	5	200

Table 10: Method-specific hyperparameters. Columns: α_A AdamW learning rate for the up-projection A (and for the entire adapter on non-Stiefel methods); α_B Cayley-Adam learning rate for the Stiefel-constrained down-projection B ; K layer budget (out of L transformer layers); N number of mini-batches used to estimate the Fisher score; n_c Cayley inner iterations; T_{qr} QR re-projection period (in optimizer steps). All methods share a common training schedule: batch size 16, gradient accumulation 4, weight decay 0.01, AdamW $(\beta_1, \beta_2) = (0.9, 0.999)$, three epochs over Commonsense-170K, sequence length 256, bf16, $r = 32$, $\alpha = 64$, target modules $\{q, k, v, \text{up}, \text{down}\}$. The Stiefel learning rate $\alpha_B = 10^{-3}$ was tuned on a held-out subset of LLaMA-3.2-3B and used unchanged across all backbones.

G Single-Backbone Deep Dive: LLaMA-3.2-3B with Four Seeds

The cross-architecture ablation in Table 2 (and its full-twelve-backbone version in Table 7) reports a single seed for the largest backbones. To complement that breadth with a higher-statistical-power deep dive on a single backbone, we re-run the four-way ablation on LLaMA-3.2-3B with four seeds. Table 11 reports WikiText-2 perplexity at $K = L/2$ over the full Commonsense-170K training set.

Method	Fisher	Stiefel	Params (M)	PPL
LoRA-all	no	no	33.0	10.520 ± 0.07
FG-LoRA	yes	no	16.5	9.140 ± 0.05
Stiefel-LoRA	no	yes	33.0	8.168 ± 0.04
FoRA (Ours)	yes	yes	16.5	7.654 ± 0.05

Table 11: 2×2 ablation on LLaMA-3.2-3B with $K = L/2$ (full Commonsense-170K, four seeds, mean \pm std). The two components combine super-additively. FoRA reaches the lowest perplexity at half of the parameter count of LoRA-all and Stiefel-LoRA.

Each component is helpful in isolation: Fisher selection alone (FG-LoRA) reduces perplexity from 10.52 to 9.14 at half the parameters, and the Stiefel constraint applied alone (Stiefel-LoRA) reduces it from 10.52 to 8.17 at the same parameter budget. The full FoRA reaches 7.65, outperforming both. The gain from adding Stiefel to Fisher selection (FG-LoRA \rightarrow FoRA, -1.49) is larger than the gain from removing Fisher selection while keeping Stiefel (Stiefel-LoRA \rightarrow FoRA, -0.51) per unit of parameter saved, which is consistent with our motivation: when the layer budget is reduced, each remaining adapter must use its rank to the fullest, so the Stiefel constraint becomes more impactful precisely in the selective setting.

H Cross-Model Generalization of Stiefel Mechanism and K-Sensitivity

Sections 5.2 and 5.3 report the K-sensitivity analysis and Stiefel rank-preservation mechanism on LLaMA-3.2-3B. This appendix verifies that the same qualitative patterns hold for two additional backbones from different model families: Gemma-3-1B-pt (Gemma-3 family, 26 layers) and Qwen3-4B (Qwen3 family, 36 layers).

K-sensitivity (Gemma-3-1B-pt). Figure 4 replicates the K-sweep of Section 5.2 on Gemma-3-1B-pt, sweeping the layer budget K across five values covering 25%–100% of the 26 transformer layers. The

result reproduces the LLaMA-3.2-3B pattern: FG-LoRA (Fisher selection without Stiefel) degrades monotonically as K increases beyond the Fisher-selected core, while FoRA remains essentially flat across the full sweep range, with variation contained within the two-seed error band. This confirms that the K -robustness of FoRA is not specific to the LLaMA architecture.

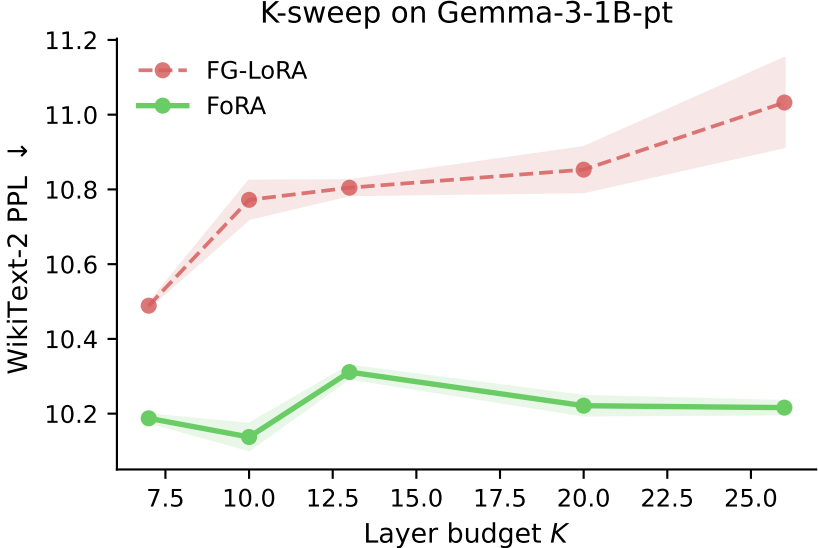


Figure 4: Sensitivity to layer budget K on Gemma-3-1B-pt (26 layers), evaluated by WikiText-2 PPL. $K \in \{7, 10, 13, 20, 26\}$. FoRA remains flat across all K values; FG-LoRA degrades as K increases beyond the Fisher-selected core. Mean \pm half-range over two seeds.

Stiefel rank-preservation (Qwen3-4B and Gemma-3-1B-pt). Figure 5 replicates the singular spectrum analysis of Section 5.3 on Qwen3-4B and Gemma-3-1B-pt. In both cases, the unconstrained methods (LoRA-all, FG-LoRA) produce adapters whose singular values decay rapidly from index $i = 1$, converging to a mean effective rank of $0.67\text{--}0.77 \times r$. The Stiefel-constrained methods (FoRA, Stiefel-LoRA) maintain a near-flat plateau across all r singular values and recover effective rank to $0.88\text{--}0.94 \times r$. The pattern is consistent across all four target module types shown and matches the LLaMA-3.2-3B result in Section 5.3, indicating that effective-rank preservation by the Stiefel constraint is a structural property that transfers across model families.

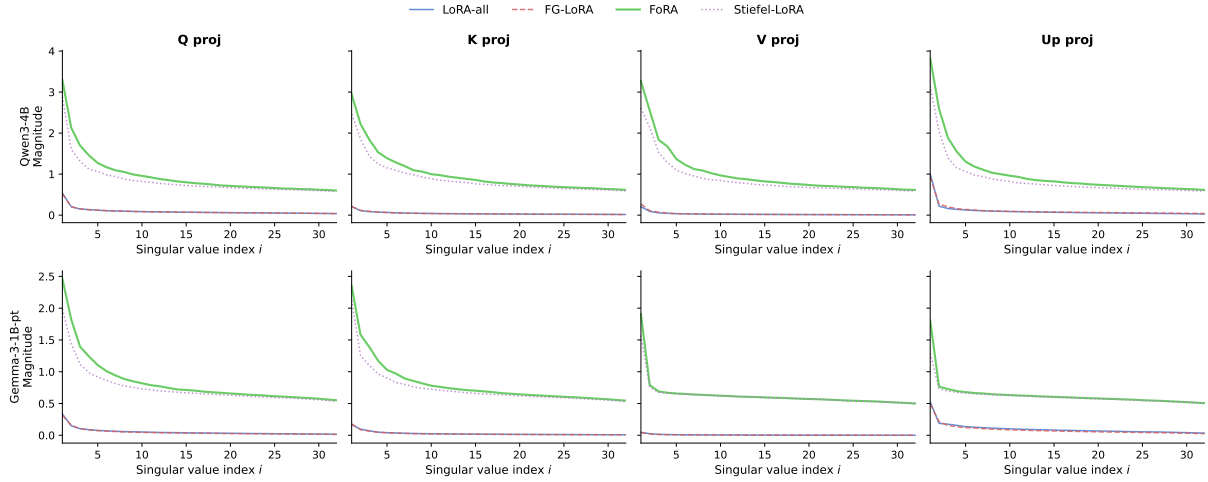


Figure 5: Singular spectrum of $\Delta W = BA$ across four target module types on Qwen3-4B (top row) and Gemma-3-1B-pt (bottom row), with $r = 32$. Stiefel-constrained methods (FoRA, Stiefel-LoRA) maintain a near-uniform plateau up to index $i = r = 32$; unconstrained methods (LoRA-all, FG-LoRA) decay from the first index, indicating rank underutilization. Each curve is averaged across all layers of the respective module type.